Optical STEM detection for scanning electron microscopy

Kievits, Arent J.; Duinkerken, B. H.Peter; Fermie, Job; Lane, Ryan; Giepmans, Ben N.G.; Hoogenboom, Jacob P.

DOI
10.1016/j.ultramic.2023.113877

Publication date
2024

Document Version
Final published version

Published in
Ultramicroscopy

Ultramicroscopy 256 (2024) 113877

Contents lists available at ScienceDirect

Ultramicroscopy

journal homepage: www.elsevier.com/locate/ultramic

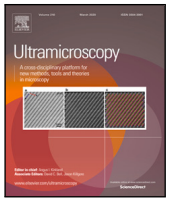

Optical STEM detection for scanning electron microscopy

Arent J. Kievits [a,*], B.H. Peter Duinkerken [b], Job Fermie [c], Ryan Lane [a], Ben N.G. Giepmans [b], Jacob P. Hoogenboom [a]

[a] Department of Imaging Physics, Delft University of Technology, Delft, The Netherlands
[b] Department of Biomedical Sciences of Cells and Systems, University Medical Center Groningen, University of Groningen, Groningen, The Netherlands
[c] Delmic B.V., Delft, The Netherlands

ARTICLE INFO

Dataset link: https://data.4tu.nl/datasets/9c98aee1-608e-4c71-8b89-dcb1e8eb3e5e

Keywords:
Scanning electron microscopy
Scanning transmission electron microscopy
Electron detection
Volume electron microscopy
Instrumentation development

ABSTRACT

Recent advances in electron microscopy techniques have led to a significant scale up in volumetric imaging of biological tissue. The throughput of electron microscopes, however, remains a limiting factor for the volume that can be imaged in high resolution within reasonable time. Faster detection methods will improve throughput. Here, we have characterized and benchmarked a novel detection technique for scanning electron microscopy: optical scanning transmission electron microscopy (OSTEM). A qualitative and quantitative comparison was performed between OSTEM, secondary and backscattered electron detection and annular dark field detection in scanning transmission electron microscopy. Our analysis shows that OSTEM produces images similar to backscattered electron detection in terms of contrast, resolution and signal-to-noise ratio. OSTEM can complement large scale imaging with (scanning) transmission electron microscopy and has the potential to speed up imaging in single-beam scanning electron microscopes.

1. Introduction

Electron microscopy (EM) of tissues and cells has gained a significant track record in the past twenty years due to improvements in methodology. Volumetric reconstructions with a resolution of several nanometers offer insight into biological function at different organizational scales. However, the low inherent throughput of electron microscopes still restricts the applications of most studies to volumes smaller than 10^6 μm^3 [1,2]. Recent efforts have focused on improving the throughput by automating sample collection and loading [3–5], parallelization of sample processing and simultaneous acquisition on multiple instruments [6–11] and reducing overhead and increasing the autonomy of acquisition platforms [4,7,9–12]. Throughput can be increased by more than an order of magnitude with multibeam scanning electron microscopy (MB-SEM), in which the sample is scanned in parallel with an array of beams in a single instrument [13–15].

Still, the acquisition speed in every technique remains fundamentally limited by the theoretical minimum exposure time, electron beam current, magnification, and sample contrasting (i.e. staining) needed to obtain images that are suitable for biological interpretation. Electron collection and detector efficiencies further define the practical limit. The detector orientation determines to a large extent the collection efficiency, although immersive magnetic or electrostatic fields may further influence both factors [16]. The detector efficiency is determined by the internal layout of the detector. In segmented backscattered and transmission electron detectors, semiconductor materials form the active layer for conversion of the electron signal into a measurable current [17]. In such a setup, the detection efficiency is dependent on the electron energy. For biological SEM with beam energies optimized for contrast, both the electron yield and detection efficiency are typically low. This implies relatively long pixel dwell times (>2 μs). Nevertheless, optimization of detection conditions of backscattered imaging in a scanning electron microscope (SEM) can reduce acquisition times up to 20-fold [18].

Transmission imaging may be preferred for imaging ultrathin biological samples in a conventional SEM [19,20], as this can yield a higher signal-to-noise ratio (SNR) and improved dynamic range [20]. As an alternative to grid supports, the sample can instead be placed on a scintillator that directly converts the transmission signal into a photon signal. This photon signal can then be measured with a photon detector, as employed previously to image whole cells grown on a scintillator surface [21]. Development of a MB-SEM for imaging ultrathin biological specimens has further motivated transmission imaging with

Abbreviations: OSTEM, Optical scanning transmission electron microscopy; SE, Secondary electron detection; BSD, Backscattered electron detection; BSD-SB, Backscatter electron detection with negative stage bias potential; ADF-STEM, Annular dark-field scanning transmission electron microscopy; LE, Electron beam landing energy; SNR, Signal-to-noise ratio

* Corresponding author.
E-mail address: A.J.Kievits@tudelft.nl (A.J. Kievits).

https://doi.org/10.1016/j.ultramic.2023.113877
Received 12 July 2023; Received in revised form 13 October 2023; Accepted 21 October 2023
Available online 30 October 2023

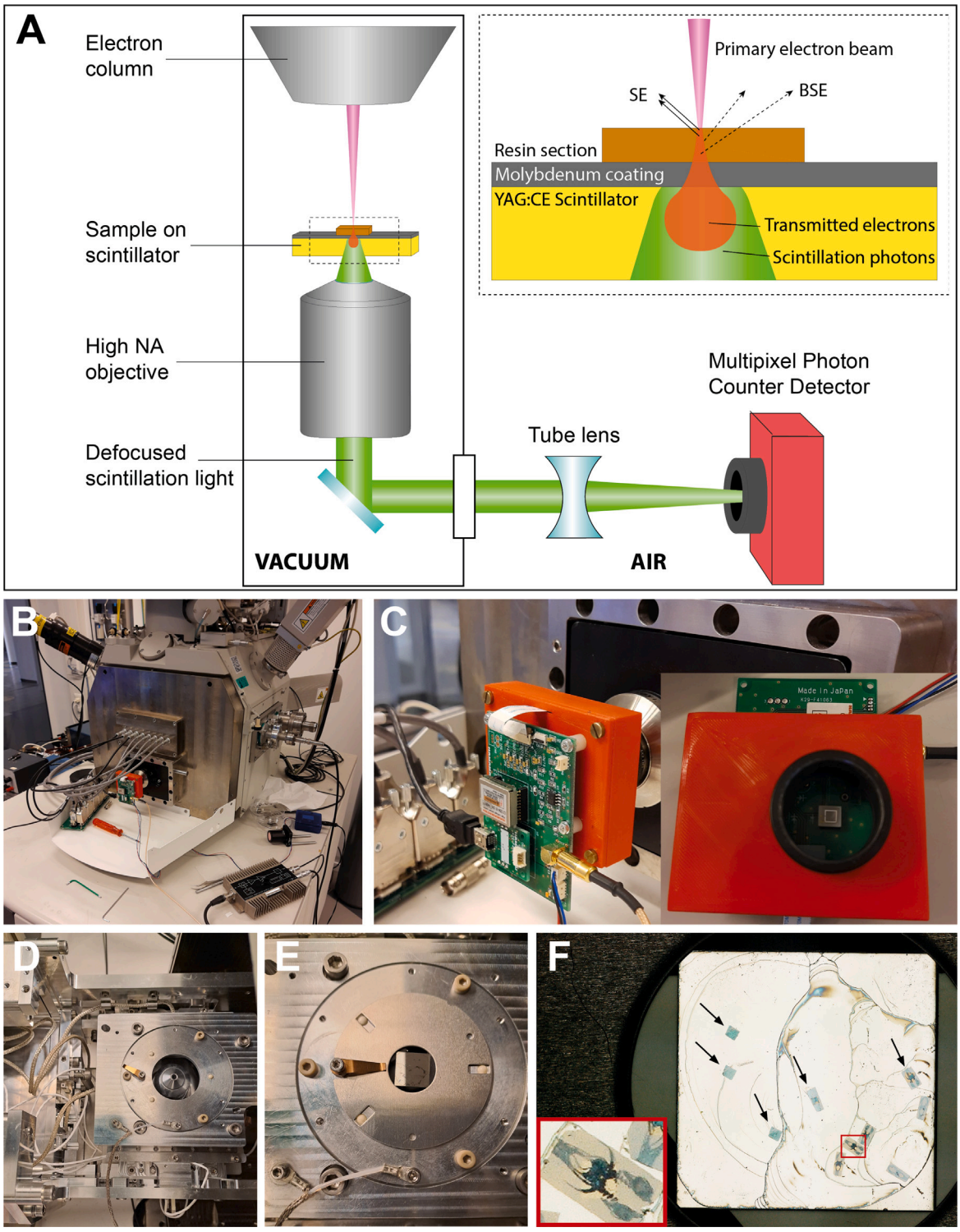

Fig. 1. Optical scanning transmission electron microscopy (OSTEM). **A**: Schematic illustration of the imaging scheme and substrate. The electrons transmit through the sample and molybdenum layer, generate photons in the scintillator which are captured by the objective and projected onto the MPPC (outside the vacuum). **B**: The integrated microscope with the SECOM fluorescence microscope modified for OSTEM detection. **C**: Multipixel photon counter (MPPC). **D**: Sample stage with top plate and objective. **E**: Sample ring holding the scintillator substrate with the sections. **F**: Reflected light microscopy image of zebrafish sections on scintillator.

a scintillator. It allows for straightforward separation of the individual signals compared to secondary electron (SE) or backscattered electron detection (BSD) [15,20]. The contrast in this imaging scheme depends on the transmission coefficient of the sample, providing a readout of the electron density of the specimen.

Here, we present a detailed investigation and benchmarking of this detection technique for SEM, which we name optical scanning transmission electron microscopy (OSTEM). Of particular interest for EM applications is the fastest imaging rate that can be achieved without compromising on image quality. We find that the signal-to-noise ratio of OSTEM images exceeds that from most conventional SEM detection techniques for short (<1 μs) dwell times. Moreover, SEM imaging of zebrafish and rat pancreas tissue with OSTEM yields images with similar contrast and SNR as BSD.

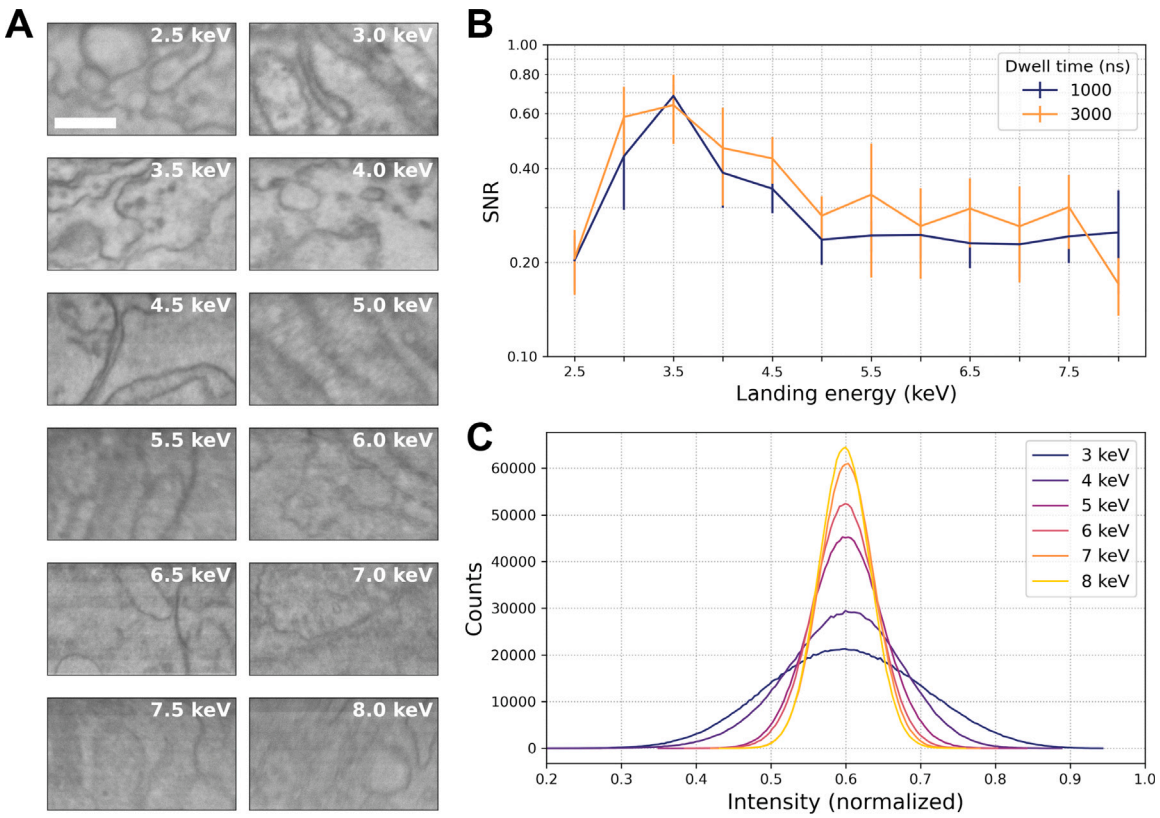

Fig. 2. Landing energy optimization of OSTEM. **A:** Images taken with increasing landing energy (increments of 0.5 keV) but fixed 3 µs dwell time and 0.4 nA beam current. Scale bar: 500 nm. **B:** Mean SNR with standard deviation of images per landing energy, showing a peak at 3.5 keV. A single SNR value is calculated for each image by averaging the SSNR over the full frequency spectrum Unser et al. [23]. **C:** Intensity histograms of images in **A** (median corrected), illustrating a decrease in contrast for higher landing energies.

2. Results and discussion

2.1. Single beam optical scanning transmission electron microscopy (OSTEM)

In OSTEM, ultrathin biological sections are directly placed on a thin film-coated, cerium-doped single-crystal yttrium aluminum garnet (Ce:YAG) scintillator (Fig. 1A). The thickness of the scintillator crystal (0.15 mm) ensures the objective lens correction collar can be used, while not making the scintillators too thin and thus too fragile for use during sample preparation. OSTEM is implemented in a modified integrated fluorescence microscope (SECOM [22], Fig. 1B); the impinging focused electron beam transmits through the sample and coating layer to reach the scintillator. The resulting photon signal from the scintillator is collected by an air objective and projected onto a multipixel photon counter situated outside of the vacuum (Fig. 1C). The geometry of the SECOM, with the objective directly situated under the sample carrier (Fig. 1D-E), allows for a high collection efficiency. Prior to EM, low magnification images are taken with a digital light microscope to guide navigation and region-of-interest selection inside the SEM (Fig. 1F).

2.2. Optimizing OSTEM landing energy

Before comparing OSTEM to other detection techniques, we experimentally determined the optimal landing energy (LE) by acquiring images of zebrafish larval tissue at increasing landing energies (Fig. 2A) and measuring the SNR and image histograms (Fig. 2B-C). The SNR is expected to increase with the LE due to the generation of more signal photons per electron. Images under 2.5 keV were not recorded because the recorded photon signal was too low. The SNR rises with increasing landing energy until it peaks at 3.5 keV (Fig. 2B). The trend in the histograms, towards a narrower spread in intensity values (Fig. 2C), corresponds to the qualitative observation that the image contrast seems to visually deteriorate (Fig. 2A) for landing energies higher than 4 keV. This is accompanied by a decrease in SNR. Based on these results and the fact that the resolution is expected to increase with the landing energy, we chose 4 keV as the landing energy for all subsequent experiments unless noted otherwise.

2.3. Qualitative comparison to backscattered electron imaging

After determining the optimal LE for OSTEM, we then acquired OSTEM and BSD images of rat pancreas and zebrafish larval tissue with different LEs and detectors but otherwise identical acquisition parameters. The image contrast for BSD was experimentally found to be best at 2 keV LE (rat pancreas) and 1.5keV (zebrafish) respectively. A comparison between inverted BSD images and OSTEM images shows apparent similar contrast (Fig. 3). BSD and OSTEM resolve the same ultrastructural details, such as insulin granules in the islet of Langerhans of the rat (arrows in inset top row of Fig. 3) and mitochondrial cristae in the zebrafish larval liver (arrows inset bottom row), demonstrating the qualitative similarity between images obtained with both detection methods.

2.4. Characterization of background texture in OSTEM

Of particular concern is the background texture in OSTEM resulting from a non-uniform detection efficiency of the scintillator across the field-of-view. To address differences in and between individual scintillator plates, images were acquired simultaneously using OSTEM, BSD, and secondary electron detection (SE) (Fig. S1). To isolate the

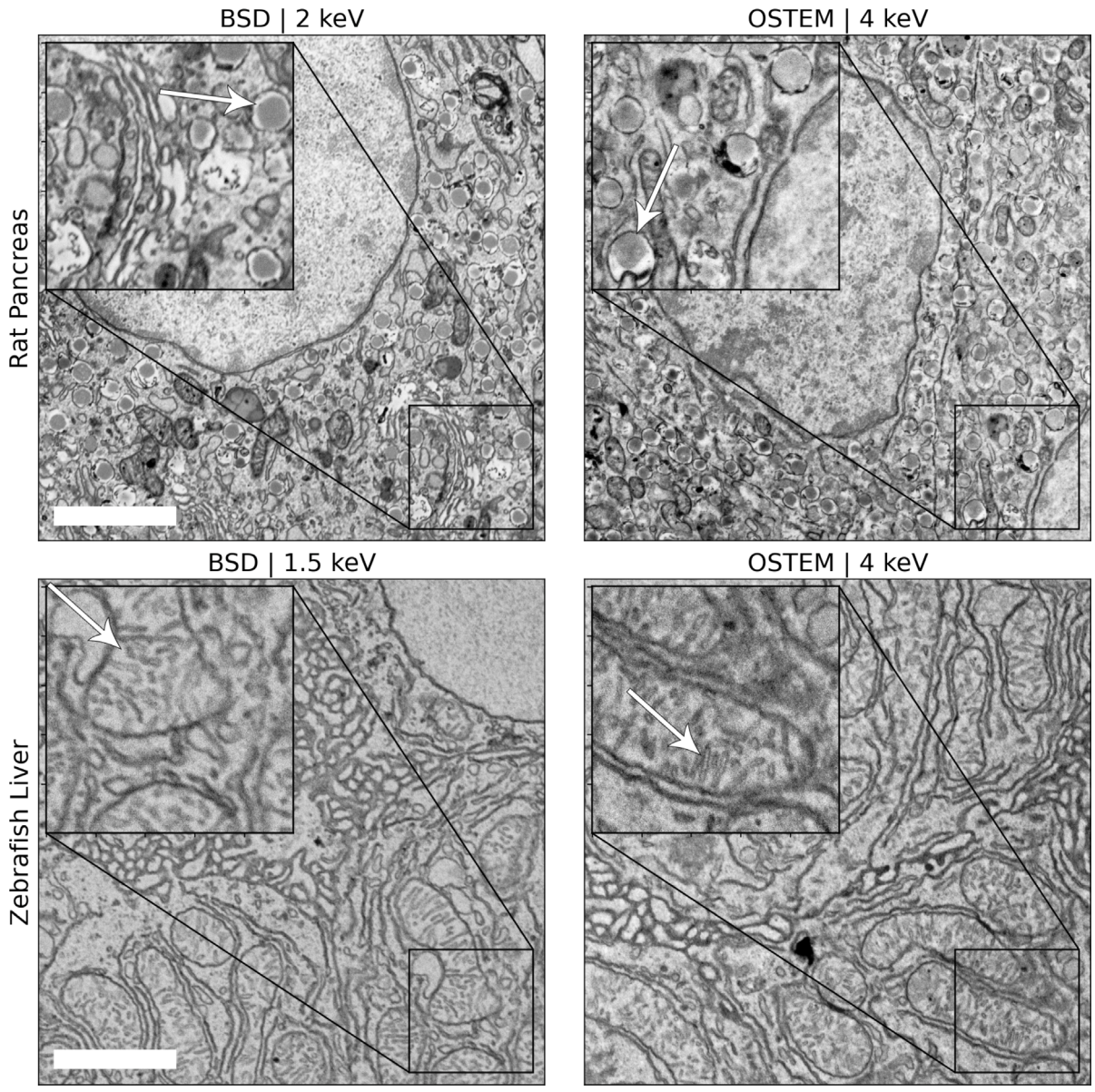

Fig. 3. Qualitative comparison of OSTEM versus BSD imaging (inverted contrast). The data were acquired from rat pancreas (top row) prepared with rOTO protocol and zebrafish larval liver tissue (bottom row) prepared with reduced osmium and *en bloc* NdAc staining. Images were acquired with 4 nm pixel size, 10 µs dwell (top row), 5.1 µs dwell (bottom row), and 0.4 nA beam current. Scale bar: 2 µm.

background texture, the substrate without tissue was imaged. For three different scintillator plates, each using similar detection settings, images were acquired 50 µm apart to illustrate large-scale spatial differences in the scintillator efficiency. A Gaussian filter with a large sigma was then applied to blur out smaller scale variations caused by surface defects. Subsequently, the remaining intensity variations were measured (Table S1).

Within every scintillator plate, the difference between the minimum and maximum image intensity was not larger than 12% of the mean, with two scintillator plates exhibiting differences below 5%. To account for outliers, the standard deviation over the mean intensity was calculated, which yielded a maximum intensity spread of 2.6%, 1.5%, and 0.80%, respectively. Thus, the background texture caused by variations in detection efficiency within the scintillator is low. Notably, we observed that one scintillator exhibited a mean intensity approximately 20% higher than the other two, despite the use of nearly identical detection settings.

2.5. Quantitative comparison to other detection methods

We then performed a systematic comparison to other detection methods: BSD with and without the use of a negative stage bias potential (BSD-SB and BSD respectively) and secondary electron detection (SE). Additionally, the results were compared with annular dark field detection in a scanning transmission electron microscope (ADF-STEM). The performance was quantified by acquiring images of zebrafish tissue with increasing dwell times (Fig. 4A) and evaluating the SNR (Fig. 4B) in both field-free and immersion modes of the SEM.

It was found that the short dwell time (<1 µs) images from OSTEM, SE and ADF-STEM are characterized by streaking. Streaking appears at fast scan rates and can originate from both the detector or readout electronics response and scintillator afterglow [24,25]. Signal from the previous scan position is carried on to the next, which results in artifacts parallel to the scan direction. This translates to a vertical band in the Fourier transform of the image (Fig. S2). The method for

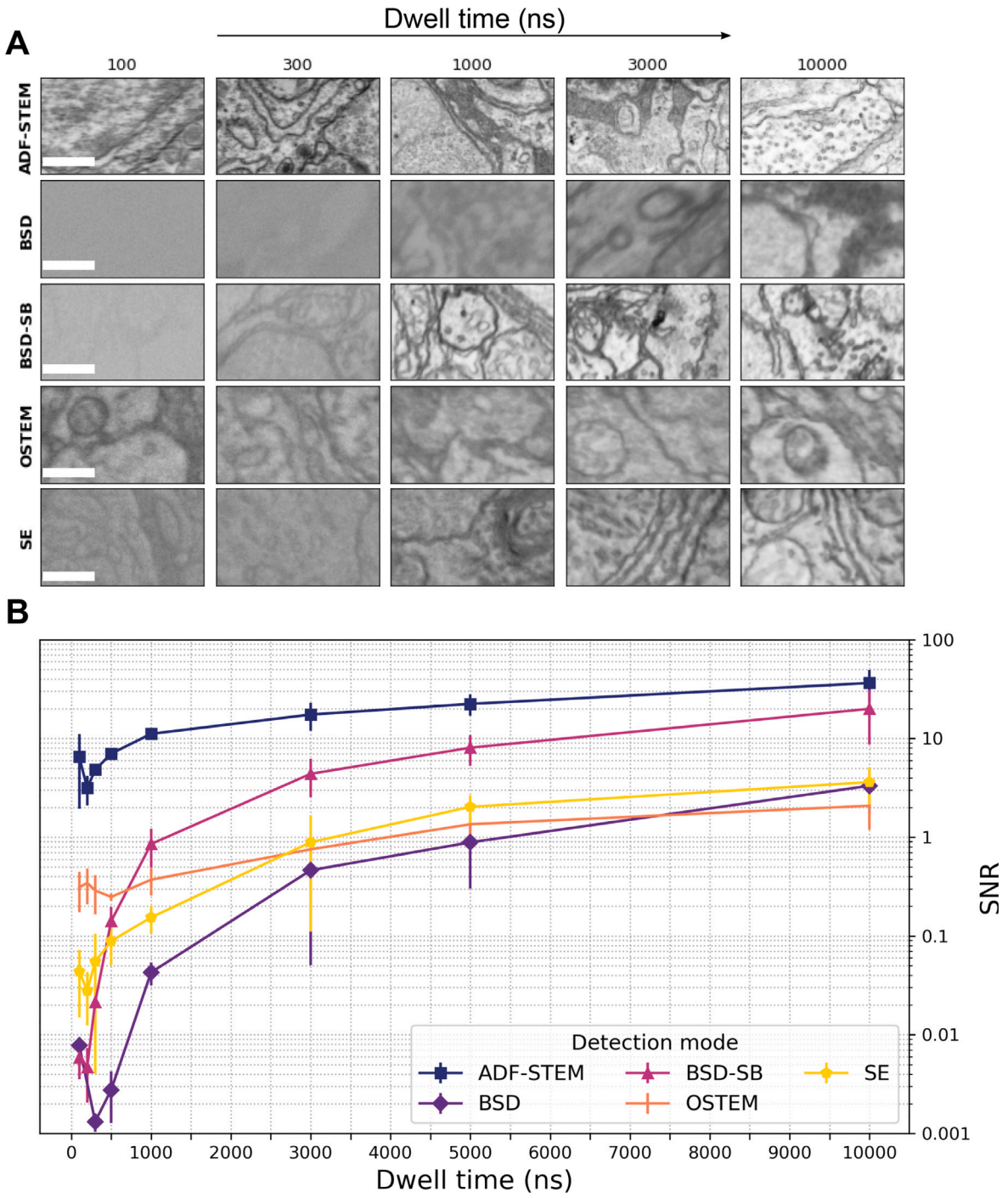

Fig. 4. Quantitative comparison of OSTEM to other detection methods. **A**: Representative high magnification images taken with different detectors at increasing dwell times. Scale bars: 500 nm. Intensity values of all images are min–max normalized from the original 16-bit range (8-bit for ADF-STEM). **B**: Mean SNR and standard deviation of images in **A**. BSD: Backscattered electron imaging (1.5 keV LE). BSD-SB: Backscattered electron imaging with a −1 kV negative stage bias (1.5 keV keV LE). OSTEM: optical scanning transmission electron imaging (4 keV LE). SE: secondary electron imaging (1.5 keV LE). ADF-STEM: annular dark field scanning transmission detection, performed in a separate microscope (25 keV LE). Contrast was inverted for BSD, SE and BSD-SB. All images were acquired with a 400 pA beam current, except for ADF-STEM (345 pA).

calculating the SNR by Lane et al. [18] is sensitive to streaking as it uses adjacent lines (which have correlated signal) parallel to the scan direction. Streaking artificially increases the correlated signal, therefore leading to a false SNR value (Fig. S3). To circumvent this, only adjacent image lines orthogonal to the scan direction were compared.

The SNR values of OSTEM, BSD and SE images were found to be comparable. Moreover, the SNR for images with short (<1 µs) dwell times is higher for OSTEM than for all other detection methods except ADF-STEM. At longer dwell times, however, the SNR of BSD-SB images increases significantly, outperforming BSD, SE as well as OSTEM. Overall, ADF-STEM yielded images with the highest SNR. The trends and relative differences for the immersion mode were similar (Fig. S4).

While the trends of the SNR curves appear similar between the different detectors, there are subtle differences. The SNR curves for OSTEM and SE remain constant at short dwell times (<1 µs) and then start to gradually increase for longer dwell times (>1 µs), while the SNR

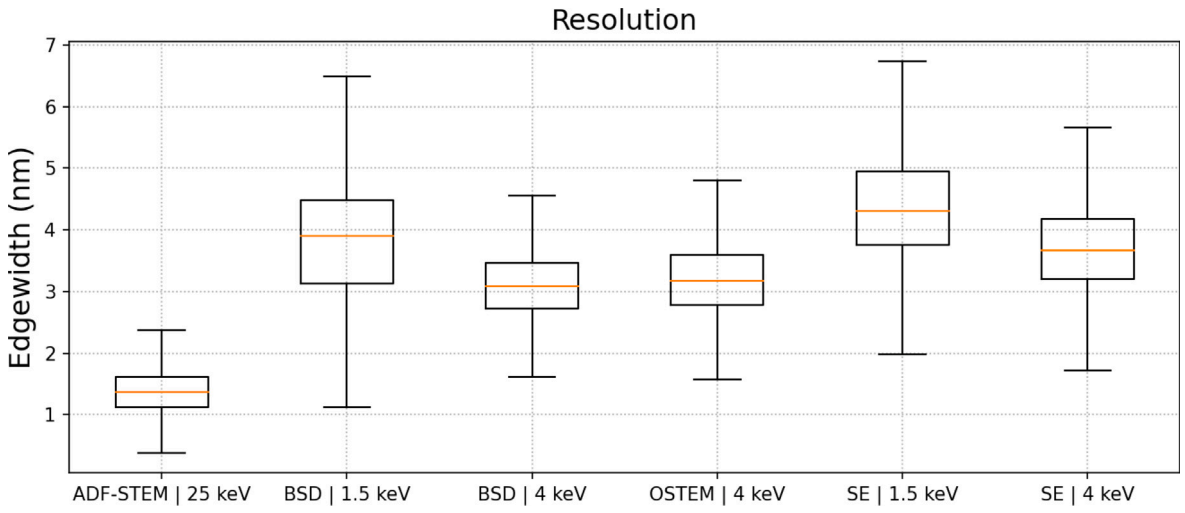

Fig. 5. Comparison of measured 35%–65% edge width distributions of detection methods on 20 nm gold nanoparticles. Box plots depict the median value (in orange), 1st and 3rd quartile (vertical box edges) and the first and 3rd quartile minus 1.5 times the inter-quartile range (whiskers). OSTEM has a higher image resolution than BSD with 1.5 keV landing energy.

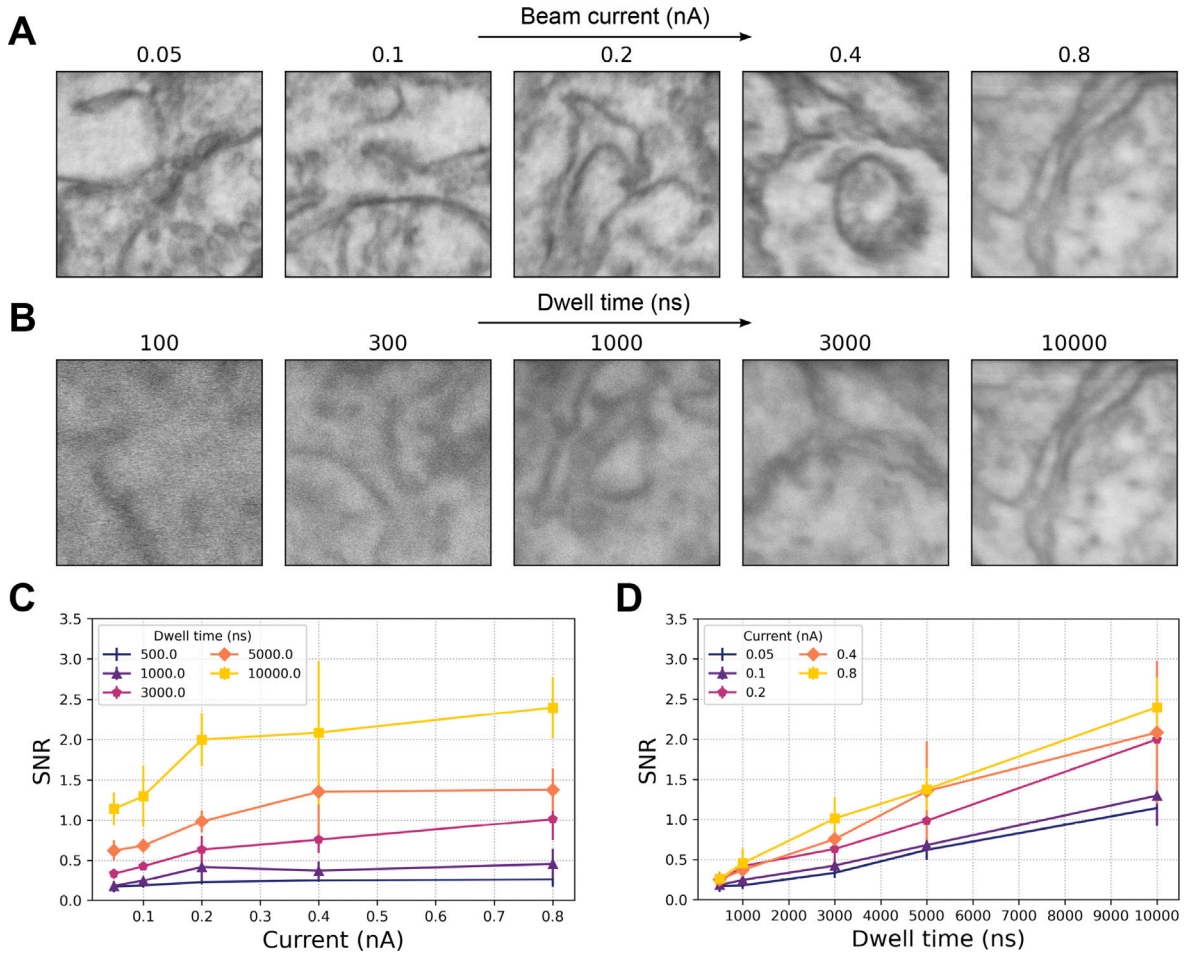

Fig. 6. Relationship between dwell time, beam current and SNR in OSTEM. **A**: OSTEM images with increasing beam current and fixed dwell time (10 µs). **B**: OSTEM images with increasing dwell time and fixed beam current (0.8 nA). **C**: Mean SNR and standard deviation of images with increasing beam current showing a stagnation of the SNR. **D**: Mean SNR and standard deviation of images with increasing dwell time, showing that the SNR keeps increasing. The used landing energy is 4 keV.

for BSD, BSD-SB and ADF-STEM consistently increases with dwell time. Only for dwell times longer than 1 µs do the SNR curves follow a similar trend, albeit with different absolute values.

Following the SNR measurements, the image resolution of OSTEM was measured and compared to the other detection methods considered. Factors that determine the image resolution are the probe size of the SEM, the electron–sample interaction, SNR and pixel size [26]. By choosing a pixel size smaller than the probe size and a long dwell time, the image resolution should only depend on the probe size and electron–sample interaction. Popular methods by which the resolution can be determined are measuring the separation between two adjacent objects and recording a line profile of the signal across a sharp (knife) edge. Traditionally this is done on a high contrast sample such as gold-on-carbon. Because an electron-transparent sample is required for OSTEM, 20 nm gold colloid particles were used instead. A knife edge experiment was then approximated by determining the distance between two percentiles of a line intensity profile over these particles, also called the edge width. To minimize the effect of their spherical shape, the 35% and 65% percentiles were chosen. The edge width was calculated for various detection methods and landing energies in immersion mode (Fig. 5), as this yields the smallest probe size and thus the best resolution possible. It was found that OSTEM provides slightly higher image resolution than BSD (4 keV vs 1.5 keV LE). Indeed, OSTEM provides nearly identical image resolution to BSD at 4 keV LE. SE images yielded lower image resolution than OSTEM and BSD.

2.6. Local saturation in the OSTEM scintillator

In OSTEM, the transmitted electron beam directly generates a photon signal by electron scattering in the scintillator. Signal generation thus occurs in a tightly confined volume in the scintillator approximately equal to the electron interaction volume of a focused electron beam. In fact, the focused electron beam interaction volume extends from the ultrathin tissue sample through the conductive coating layer into the scintillator. Signal generation in the scintillator thus occurs in the lower part of the interaction volume (see also inset in Fig. 1A). A higher density of electron scattering events may possibly lead to local saturation of the scintillator, thus the signal generation could be sensitive to the beam current.

The current and dwell time dependence of the OSTEM signal was therefore assessed as reflected by the SNR (Fig. 6). Series of images were acquired with either increasing beam currents and a fixed dwell time (Fig. 6A), or increasing dwell times and a fixed current (Fig. 6B). By definition, the SNR is expected to increase by $\sqrt{N}$ for an N-fold increase in either beam current or dwell time. The signal generation is proportional to the total number of scattering events, which increases with both the beam current and dwell time. The relationship between the SNR and dwell time or beam current is therefore expected to be similar. However, with an increasing beam current but fixed dwell time, the experimental SNR consistently stagnates for currents of 0.4 nA and larger (Fig. 6C). When increasing the dwell time and keeping the beam current constant, the SNR keeps increasing, following the expected trend for the theoretical SNR (Fig. 6D). Thus, increasing the beam current does not have the same effect on the SNR as increasing the dwell time.

3. Discussion

The deposition of ultrathin sections directly onto a scintillator substrate is a viable alternative to placing tissue on thin foil spanned across grid, as traditionally performed in (S)TEM. The TEM grid bars obscure parts of the sample potentially leading to missing data, though a single slot grid can be used to circumvent this. Nevertheless, the scintillator provides a much larger unobstructed area of view in comparison to a single slot grid. This allows the collection and imaging of more sections on a single substrate. Thus, placing ultrathin sections on a scintillator substrate for OSTEM is suitable for high throughput applications.

The determined optimal landing energy of 4 keV is the same energy at which the product of the simulated SNR and contrast-to-noise ratio (CNR) was previously found to be maximized [20]. It should be noted that this optimum may shift somewhat depending on the specific sample composition, staining, section and coating thickness. The relation between the landing energy and the SNR and image contrast is not trivial. Similar to Zuidema and Kruit [20], a stabilization of the SNR beyond 5 keV is observed. While we report a lower absolute SNR, shorter dwell times, a lower beam current and a different tissue with less heavy metal staining were used. The sample from Zuidema and Kruit [20] consists of tissue on a TEM grid fixed onto a different type of scintillator and coating. These factors all have an effect on the final SNR and contrast.

We addressed to what extent the added background texture of the scintillator influences OSTEM image quality. The contribution from the non-uniform detection efficiency of the scintillators is acceptably low, but notable differences in mean intensity may exist between individual scintillator plates. The latter observation implies a variance in total photon yield, possibly attributable to differences in crystal growth conditions. In BSD and SE imaging schemes, the electron energy is chosen such that most of the scattering events take place in the biological section and thus the substrate's underlying surface topography is not revealed. In ADF-STEM, the biological section lies on a formvar layer, which is electron-transparent at 25 keV beam energy. While the SE images reveal some surface defects, these are less pronounced in OSTEM. We attribute this to the different contrast mechanism in OSTEM, which is less sensitive to surface roughness than SE. Furthermore, the electron beam will spread in the biological section, thereby blurring out defects in the underlying substrate. Thus, the contribution of the substrate surface to the total background texture is minimal. Nonetheless, the polishing quality of the scintillator is important in minimizing the background texture.

In our experiment, the SNR of BSD-SB outperformed OSTEM for dwell times longer than 1 µs. At shorter dwell times, however, OSTEM outperforms BSD with and without a bias potential. This suggests that transmission imaging is the preferred option when biasing the sample (or alternatively the detector) is not an option. Similarly, ADF-STEM outperforms OSTEM as its 25 keV energy electrons generate more signal. Furthermore, it was established that streaking leads to a false signal-to-noise value for short dwell time images. In practice, the dwell time should be several times the scintillator decay constant to minimize the streaking contribution to the signal. Scintillators with shorter decay times are available, but the luminescence wavelength must be compatible with the optical components and detector.

It was found that OSTEM provides slightly higher resolution than BSD. This is attributed to decreased chromatic aberration due to the higher primary beam energy. We attribute the lower resolution of SE compared to OSTEM mainly to the contribution of so called SE2s, i.e. SEs generated by backscattered electrons, which are emitted from a larger area around the primary beam incident point. Furthermore, SEs may diffuse through the material before being emitted. Therefore, the position where the SEs originate from may be slightly different from the primary beam position, which for BSD has a more direct relation.

The image quality in SEM is not only determined by the SNR and resolution, but also the contrast-to-noise ratio (CNR). However, no reliable method exists to estimate the CNR from tissue since no two positions in the sample will have the same composition. Furthermore, the detector gain has to be adjusted between landing energies, further influencing the CNR. It is therefore impossible to compare the CNR between images acquired at different landing energies.

The image quality in OSTEM can be further improved. The main limiting factors are possible local saturation of the scintillator and the high backscattered electron coefficient of the molybdenum coating

layer. In the interaction volume, energy is deposited very inhomogeneously with most electron scattering occurring below the electron beam focus. Thus, for the scintillator, most electron scattering events are expected just below the coating layer, which may in turn lead to strongly localized energy deposition. In the scintillator material, the photon signal is generated by energy transfer to the active Ce dopants [27], which for high local energy density may be prone to additional energy loss. We found indirect evidence that this leads to a sub-linear increase of the photon signal and hence a partial saturation of the light output. Also, the finite doping concentration and decay time of the Ce atoms may limit the transfer of electron energy into photon signal leading to signal saturation. The degree of saturation is not only influenced by the beam current, but also by the beam energy and the coating layer composition and thickness. The latter influences how much the electrons spread out before hitting the scintillator, thus determining the extent of saturation. Lastly, charging below the coating layer may play a role since the scintillator itself is non-conductive.

A full explanation and prediction of the expected SNR as a function of the dwell time, beam current, landing energy and other experimental parameters such as the coating thickness would be beneficial for finding optimized conditions. However, this requires an extensive physical model of the signal generation process, including electron scattering, transport of excited energy, conversion, quenching and saturation. This is a subject of future research. A thorough understanding of the signal and noise contributions in OSTEM and subsequent optimization may further improve throughput and lead to faster possible scanning speeds in single-beam and multi-beam scanning electron microscopes.

4. Materials & methods

4.1. Biological sample preparation

4–4.5 dpf zebrafish larva were fixed overnight in 2% glutaraldehyde (GA) and 2% paraformaldehyde (PFA) in 0.1 M sodium cacodylate buffer (SCB) at 4 °C. Subsequently, the fish were post-fixed in 1% osmium tetroxide and 1.5% potassium ferrocyanide for 2 hr in 0.1M SCB. Next, *en bloc* staining was performed with 4% neodymium acetate in MilliQ for 30 min at RT. The neodymium acetate was pre-spun at 21.000 g for 5 min [28]. Between each step, the samples were washed 3 times for 5 min each using MilliQ at RT. Afterwards, the tissue was dehydrated in 30%, 50%, 70% ethanol (10 min per step at RT), followed by dehydration in absolute ethanol (10 min, 20 min, 2 × 30 min), acetone (dried at MgSo4), 2 × 10 min, RT. The sample was then incubated with EPON:acetone mix (1:1) overnight at RT, followed by incubation with fresh EPON at 3 hr minimum at RT on the next day, then 15 min at 58 °C, followed lastly by 1 hr at 200 mbar. The fish in EPON were then oriented in moulds and left overnight at 58 °C to polymerize.

Rat pancreas was prepared according to the reduced osmium-thiocarbohydrazide-osmium (rOTO) protocol [29]. Rat pancreas was isolated, fixed overnight in 2% GA and 2% PFA in 0.1 M SCB at 4 °C and subsequently embedded in 4% agarose (in 0.1M SCB), after which 60 µm vibratome sections were cut and washed with 0.1 M SCB. The vibratome sections were post-fixed in 2% osmium tetroxide, 1.5% potassium ferrocyanide and 4 mM calcium chloride in 0.1 M SCB for 1 hr at 4 °C. Subsequently, the tissue was exposed to 0.22 µm-filtered thiocarbohydrazide for 20 min at RT followed by 2% osmium tetroxide for 30 min at RT. The tissue was further contrasted by submerging it in 2% uranyl acetate in MilliQ overnight at 4 °C. The following day, a solution of lead aspartate was made by combining 10 mL of 3 mM aspartic acid (pH 3.8) with 0.066 g of lead nitrate and adjusting the pH to 5.5 with 1N KOH. After removing the uranyl acetate, the sample was *en bloc* stained with the Walton's lead aspartate solution for 30 min at 58 °C. Between each step, the tissue was washed 3 times for 5 min each using MilliQ at RT [30]. Finally, the sample was dehydrated and embedded in EPON as described above.

4.2. Specimen preparation

80 nm ultrathin sections were cut from the embedded zebrafish larvae and rat pancreas tissue using a UC7 ultramicrotome (Leica) with a diamond knife connected to a water bath (Diatome Ltd). The sections were transferred directly onto the surface of the scintillator crystal with the help of Perfect Loop (Diatome Ltd), after which the sample was dried on a hot plate. The scintillators were stuck to a SECOM ring holder (Delmic B.V.) with a piece of carbon tape. No further coating was performed before loading the samples in the microscope. Overview images of the scintillator were taken prior to EM using a VHX-6000 digital light microscope (Keyence) operated in reflection mode.

4.3. Experimental setup

We have made several modifications to the sample substrate used by Zuidema and Kruit [20]. In this protocol, sections are transferred to a regular TEM grid which is then stuck to a boron-coated CRY-18 scintillator. In this work, cerium-doped yttrium aluminum garnet (ce:YAG) scintillator screens (Delmic B.V.) were sputter coated with a 30 nm layer of molybdenum to reduce charging and saturation. To detect scintillation photons, we use the same setup from Zuidema and Kruit [20] by modifying a SECOM integrated fluorescence microscope (Delmic B.V.) retrofitted into a Verios 460 SEM (FEI) (Fig. 1A-B) with a fixed 6 mm working distance. The emission filters of the fluorescence microscope were removed and the cMOS camera was replaced with a Hamamatsu multi-pixel photon counter (MPPC, model s13360-3050CS). A 0.95 NA air objective (Nikon) was used for photon collection. The signal from the MPPC was amplified by a DHPVA-101 voltage amplifier (Femto) with a 20–30 dB gain and 100 MHz filter before feeding it into the external detector port of the SEM.

4.4. Imaging

For OSTEM imaging, the SECOM objective was aligned to the detector with x- and y-translations using its dedicated stage. This was performed while scanning the electron beam at low magnification until the cathodoluminescence signal from the scintillator was in the center of the screen. Subsequently, the emission light was defocused on the MPPC to prevent saturation of the detector by a z-translation of the objective stage. The operating voltage of the detector, which controls the sensitivity, was set to a value between 52 and 54 V to achieve a mean intensity approximately half the bit-depth to prevent histogram clipping. BSD was performed with the retractable concentric backscattered detector (FEI), employing a 1.5 keV or 2 keV landing energy (experimentally found to produce the best images). BSD with stage bias was performed with the setup as described in Lane et al. [18], applying a −1 keV stage bias and a 2.5 keV beam energy resulting in a 1.5 keV landing energy. SE detection was performed with the Everhart–Thornley detector (FEI) in field-free mode or the through-the-lens detector (FEI, operated in SE mode) in immersion mode. SE and BSD images were acquired simultaneously for convenience.

ADF-STEM images were acquired with an annular darkfield quadrant detector, mounted in a Supra 55 SEM (Zeiss), at a fixed landing energy of 25 keV and a measured probe current of 345 pA. To prepare the sample for imaging, ultrathin sections were picked up from the water bath after sectioning with a 2 × 1 mm slot grid and placed on a metal plate with holes covered by a thin layer of formvar.

4.5. Quantitative measurements

The signal-to-noise ratio of the images was quantified by averaging the spectral signal-to-noise ratio (SSNR) [23] over the full frequency space of every electron micrograph [18]. Additionally, the SSNR was validated using a method based on cross-correlation [26]. Both methods require the pixel size to be smaller than the probe size such that

successive scan lines have a high amount of overlap in signal. A pixel size of 1 nm was used for all SEM-based detection techniques and 0.5 nm for ADF-STEM. This is several times smaller than the highest measured image resolution (3 nm for OSTEM and 1.3 nm for STEM respectively). For every measurement, the stage was moved to a fresh region in the sample. The average SNR value was taken of at least 4 images. The SSNR is calculated using the following formula:

$$SSNR(R) = \frac{\sum_{r\epsilon R} |\sum_k F_k(r)|^2}{\frac{K}{K-1}\sum_{r\epsilon R}\sum_k |F_k(r) - \overline{F}(r)|^2} - 1 \quad (1)$$

where $F_k(r)$ is the Fourier transform of the k'th image (alternating scan line), with K images (scan lines) in total. $\overline{F}(r) = \frac{1}{K}\sum_k(r)$ is the mean of the Fourier transformed images and R is the region of interest. If R is the full image, a single SNR value is obtained. R can also be a ring in Fourier space.

The image resolution of the detection techniques was estimated from 20 nm gold colloid nanoparticles (Sigma Aaldrich) directly deposited on a molybdenum-coated Ce:YAG single crystal. To approximate a knife-edge measurement, the 35%–65% edge width was determined using the software 'FEI Image' from images taken in the immersion mode of the SEM. The histogram of edge widths as produced by FEI image was exported and combined for all images acquired with a single detection technique. A pixel size 0.5 nm was used for SEM and 0.2 nm for STEM, which is several times smaller than the measured resolution. A 10 µs dwell time was used for SEM and 3 µs for ADF-STEM to obtain images with a high SNR.

CRediT authorship contribution statement

Arent J. Kievits: Performed the experiments with OSTEM, analyzed the data, drafted the manuscript and figures based on an initial proposal by J.F. and J.P.H, discussed the results, edited the manuscript.. **B.H. Peter Duinkerken:** Performed the sample and specimen preparation, performed the ADF-STEM imaging, discussed the results, edited the manuscript. **Job Fermie:** Discussed the results, edited the manuscript. **Ryan Lane:** Provided the code for the SNR analysis, assisted with the OSTEM experiments, discussed the results, edited the manuscript. **Ben N.G. Giepmans:** Supervised the work of P.D, discussed the results, edited the manuscript. **Jacob P. Hoogenboom:** Supervised the work of A.J.K, discussed the results, edited the manuscript.

Declaration of competing interest

A.J.K., P.D., J.F., R.L. and B.N.G.G. declare that they have no known competing financial interests or personal relationships that could have appeared to influence the work reported in this paper. J.P.H. is co-founder of and shareholder in Delmic BV, a company selling integrated microscopes including the SECOM used in this research.

Data availability

The data and analysis code are available via the 4TU.ResearchData repository with DOI https://data.4tu.nl/datasets/9c98aee1-608e-4c71-8b89-dcb1e8eb3e5e.

Acknowledgments

We thank Anouk Wolters from the UMC Groningen for preparing the rat pancreas sample used in this research. Part of the work has been performed in the UMCG Microscopy and Imaging Center (UMIC). This work was sponsored by ZonMW, Netherlands grant 91111.006 and the Netherlands Electron Microscopy Infrastructure (NEMI), NWO National Roadmap for Large-Scale Research Infrastructure of the Dutch Research Council (NWO 184.034.014). The work performed at Delft University of Technology was supported by an NWO-LIFT grant (ENPPS.LIFT.019.030), the EU-ECSEL program MadeIn4 (826589) and the EFRO program Kansen voor West (IMDAP), which was partly financed by EU-REACT, the EU response to the COVID-19 pandemic.

Appendix A. Supplementary data

Supplementary material related to this article can be found online at https://doi.org/10.1016/j.ultramic.2023.113877.

References

[1] C.J. Peddie, L.M. Collinson, Exploring the third dimension: Volume electron microscopy comes of age, Micron 61 (2014) 9–19.
[2] A.J. Kievits, R. Lane, E.C. Carroll, J.P. Hoogenboom, How innovations in methodology offer new prospects for volume electron microscopy, J. Microsc. 287 (3) (2022) 114–137.
[3] K. Hayworth, N. Kasthuri, R. Schalek, J. Lichtman, Automating the collection of ultrathin serial sections for large volume TEM reconstructions, Microsc. Microanal. 12 (S02) (2006) 86–87.
[4] Z. Zheng, J.S. Lauritzen, E. Perlman, C.G. Robinson, M. Nichols, D. Milkie, O. Torrens, J. Price, C.B. Fisher, N. Sharifi, et al., A complete electron microscopy volume of the brain of adult Drosophila melanogaster, Cell 174 (3) (2018) 730–743.
[5] J.S. Phelps, D.G.C. Hildebrand, B.J. Graham, A.T. Kuan, L.A. Thomas, T.M. Nguyen, J. Buhmann, A.W. Azevedo, A. Sustar, S. Agrawal, et al., Reconstruction of motor control circuits in adult Drosophila using automated transmission electron microscopy, Cell 184 (3) (2021) 759–774.
[6] K.J. Hayworth, C.S. Xu, Z. Lu, G.W. Knott, R.D. Fetter, J.C. Tapia, J.W. Lichtman, H.F. Hess, Ultrastructurally smooth thick partitioning and volume stitching for large-scale connectomics, Nat. Methods 12 (4) (2015) 319–322.
[7] C.S. Xu, K.J. Hayworth, Z. Lu, P. Grob, A.M. Hassan, J.G. Garcia-Cerdan, K.K. Niyogi, E. Nogales, R.J. Weinberg, H.F. Hess, Enhanced FIB-SEM systems for large-volume 3D imaging, Elife 6 (2017) e25916.
[8] L.K. Scheffer, C.S. Xu, M. Januszewski, Z. Lu, S.-y. Takemura, K.J. Hayworth, G. Huang, K. Shinomiya, J. Maitlin-Shepard, S. Berg, et al., A Connectome and Analysis of the Adult Drosophila Central Brain, Cold Spring Harbor Laboratory, 2020, BioRxiv.
[9] D.D. Bock, W.-C.A. Lee, A.M. Kerlin, M.L. Andermann, G. Hood, A.W. Wetzel, S. Yurgenson, E.R. Soucy, H.S. Kim, R.C. Reid, Network anatomy and in vivo physiology of visual cortical neurons, Nature 471 (7337) (2011) 177–182.
[10] W.-C.A. Lee, V. Bonin, M. Reed, B.J. Graham, G. Hood, K. Glattfelder, R.C. Reid, Anatomy and function of an excitatory network in the visual cortex, Nature 532 (7599) (2016) 370–374.
[11] W. Yin, D. Brittain, J. Borseth, M.E. Scott, D. Williams, J. Perkins, C.S. Own, M. Murfitt, R.M. Torres, D. Kapner, et al., A petascale automated imaging pipeline for mapping neuronal circuits with high-throughput transmission electron microscopy, Nat. Commun. 11 (1) (2020) 1–12.
[12] Z. Zheng, C.S. Own, A.A. Wanner, R.A. Koene, E.W. Hammerschmith, W.M. Silversmith, N. Kemnitz, D.W. Tank, H.S. Seung, Fast Imaging of Millimeter-Scale Areas with Beam Deflection Transmission Electron Microscopy, Cold Spring Harbor Laboratory, 2022, bioRxiv. 2022-2011.
[13] A. Mohammadi-Gheidari, C. Hagen, P. Kruit, Multibeam scanning electron microscope: Experimental results, J. Vacuum Sci. Technol. B, Nanotechnol. Microelectron. Mater. Process. Meas. Phenomena 28 (6) (2010) C6G5–C6G10.
[14] A. Eberle, S. Mikula, R. Schalek, J. Lichtman, M.K. Tate, D. Zeidler, High-resolution, high-throughput imaging with a multibeam scanning electron microscope, J. Microsc. 259 (2) (2015) 114–120.
[15] Y. Ren, P. Kruit, Transmission electron imaging in the Delft multibeam scanning electron microscope 1, J. Vacuum Sci. Technol. B, Nanotechnol. Microelectron. Mater. Process. Meas. Phenomena 34 (6) (2016) 06KF02.
[16] I. Müllerová, I. Konvalina, Collection of secondary electrons in scanning electron microscopes, J. Microsc. 236 (3) (2009) 203–210.
[17] A. Šakić, L.K. Nanver, T.L. Scholtes, C.T.H. Heerkens, T. Knežević, G. Van Veen, K. Kooijman, P. Vogelsang, Boron-layer silicon photodiodes for high-efficiency low-energy electron detection, Solid-State Electron. 65 (2011) 38–44.
[18] R. Lane, Y. Vos, A.H. Wolters, L. van Kessel, S.E. Chen, N. Liv, J. Klumperman, B.N. Giepmans, J.P. Hoogenboom, Optimization of negative stage bias potential for faster imaging in large-scale electron microscopy, J. Struct. Biol. X 5 (2021) 100046.
[19] J. Kuipers, P. de Boer, B.N. Giepmans, Scanning EM of non-heavy metal stained biosamples: Large-field of view, high contrast and highly efficient immunolabeling, Exp. Cell Res. 337 (2) (2015) 202–207.
[20] W. Zuidema, P. Kruit, Transmission imaging on a scintillator in a scanning electron microscope, Ultramicroscopy 218 (2020) 113055.
[21] T. Okumura, M. Shoji, A. Hisada, Y. Ominami, S. Ito, T. Ushiki, M. Nakajima, T. Ohshima, Electron tomography of whole cultured cells using novel transmission electron imaging technique, Micron 104 (2018) 21–25.
[22] N. Liv, A.C. Zonnevylle, A.C. Narvaez, A.P. Effting, P.W. Voorneveld, M.S. Lucas, J.C. Hardwick, R.A. Wepf, P. Kruit, J.P. Hoogenboom, Simultaneous correlative scanning electron and high-NA fluorescence microscopy, PLoS One 8 (2) (2013) e55707.

[23] M. Unser, B.L. Trus, A.C. Steven, A new resolution criterion based on spectral signal-to-noise ratios, Ultramicroscopy 23 (1) (1987) 39–51.
[24] J.P. Buban, Q. Ramasse, B. Gipson, N.D. Browning, H. Stahlberg, High-resolution low-dose scanning transmission electron microscopy, J. Electron. Microsc. 59 (2) (2010) 103–112.
[25] T. Mullarkey, C. Downing, L. Jones, Development of a practicable digital pulse read-out for dark-field STEM, Microsc. Microanal. 27 (1) (2021) 99–108.
[26] D.C. Joy, SMART–a program to measure SEM resolution and imaging performance, J. Microsc. 208 (1) (2002) 24–34.
[27] P. Schauer, Optimization of decay kinetics of YAG: Ce single crystal scintillators for S (T) EM electron detectors, Nucl. Instrum. Methods Phys. Res. B 269 (21) (2011) 2572–2577.
[28] J. Kuipers, B.N. Giepmans, Neodymium as an alternative contrast for uranium in electron microscopy, Histochem. Cell Biol. 153 (4) (2020) 271–277.
[29] P.S. Holcomb, B.K. Hoffpauir, M.C. Hoyson, D.R. Jackson, T.J. Deerinck, G.S. Marrs, M. Dehoff, J. Wu, M.H. Ellisman, G.A. Spirou, Synaptic inputs compete during rapid formation of the calyx of Held: A new model system for neural development, J. Neurosci. 33 (32) (2013) 12954–12969.
[30] J. Walton, Lead asparate, an en bloc contrast stain particularly useful for ultrastructural enzymology, J. Histochem. Cytochem. 27 (10) (1979) 1337–1342.